Korean J. Chem. Eng., **31**(11), 1973-1979 (2014)
DOI: 10.1007/s11814-014-0148-6

pISSN: 0256-1115
eISSN: 1975-7220

The effects of MCM-41's calcination temperature on the structure and hydrodenitrogenation over NiW catalysts

Fang Guo*,, Shaoqing Guo***, Xian-Xian Wei*,**, Xiaoxiao Wang***, Hongwei Xiang*, Zegang Qiu*,†, and Liangfu Zhao*,†**

*Institute of Coal Chemistry, Chinese Academy of Sciences, Taiyuan 030001, P. R. China
**Graduate University of the Chinese Academy of Sciences, Beijing 100039, P. R. China
***Taiyuan University of Science and Technology, Taiyuan 030024, P. R. China
(*Received 24 January 2014 • accepted 25 May 2014*)

Abstract−MCM-41 was calcined at 500, 560, 600 or 650 °C. It was used as support for NiW catalysts of hydrodenitrogenation (HDN) for quinoline in order to investigate the influences of the MCM-41's calcination temperature on the structure and the HDN performance of NiW catalysts. The NiW catalysts were characterized by XRD, N_2 adsorption-desorption, XPS, Raman, HRTEM and Py-IR techniques. The results showed that the surface area (S_{BET}), the average pore diameter (Dp) and the pore volume (Vp) of the MCM-41 increased with increase of the MCM-41's calcination temperature. The high S_{BET}, Dp and Vp were beneficial for the high dispersion of W species, the formation of appropriate nature of W species and acid sites on the catalysts. The HDN activity followed the order of NiW-650≈NiW-600>NiW-560>NiW-500, while the relative selectivity of HDN pathways was similar for all the catalysts.

Keywords: NiW Catalysts, Calcination Temperature, Hydrodenitrogenation, Quinoline

INTRODUCTION

Hydrodenitrogenation (HDN) is one of the most important reactions during hydrotreating processes of petroleum refining products because the nitrogen compounds in the products can result in the fast deactivation of hydrotreating catalysts and serious environmental pollution [1,2].

Conventional Mo or W sulfides promoted by Ni supported on alumina are utilized as HDN catalysts [3,4]. In recent years, many efforts have been aimed at improving the catalytic activity and the selectivity of the catalysts, including the change of active metal composition [5,6], the uses of different types of active metals [7,8], additives [9,10] and supports [2,11], etc. Among these, the use of different supports is one of the most promising approaches. The support of order mesoporous silica such as MCM-41 has attracted more and more attention due to the high surface areas and the homogeneous pore diameters. There are several reports available on developing high performance HDN catalysts supported on MCM-41 [11-14].

The impregnation of active compounds is frequently used for preparing HDN catalysts. Generally, prior to the impregnation of active compounds, the support is calcined at high temperature. It is recognized that the calcination temperature is one of the fundamental factors that can affect the support's nature, such as the surface area, the pore diameter and the surface property. For example, Khder found that the structural ordering of MCM-41 was improved as MCM-41 was calcined at 550 °C [15]. Chen et al. reported that the lattice contraction of MCM-41 and the loss of silanol density occurred as MCM-41 was calcined at elevated temperatures [16]. Actually, the support's property strongly affects the activity and the selectivity of the catalyst. However, little literature has been reported specifically about the performance of hydrotreating catalysts supported on the MCM-41 that was calcined at different temperatures. Moreover, it is reported that the sulfided NiW catalysts are superior to the sulfided NiMo catalysts for HDN reaction because of their high hydrogenation activity [4]. Therefore, our objective was to investigate the influences of the MCM-41's calcination temperature on the structure and the HDN performance over NiW catalysts.

The NiW catalysts were prepared with MCM-41 as support, which was calcined at temperatures of 500, 560, 600 or 650 °C. These catalysts were characterized by XRD, N_2 adsorption-desorption, XPS, Raman, HRTEM and Py-IR techniques. The catalytic performance in HDN of quinoline over the catalysts was investigated and the correlation between the structure and the catalytic performance of these catalysts in HDN of quinoline was also discussed.

EXPERIMENTAL SECTION

1. Catalyst Preparation

The MCM-41 was supplied by the Catalyst Plant of Nankai. Prior to the impregnation of active compounds, the MCM-41 was calcined in static air at 500, 560, 600 or 650 °C for 6 h, which was denoted as MCM-500, MCM-560, MCM-600 and MCM-650. The catalysts were prepared by co-impregnation method using an equilibrium-adsorption technique. In this method, a solution containing required amount of ammonium paratungstate (analytical grade) and nickel nitrate hexahydrate (analytical grade) in water was impregnated onto the MCM-41 support. After impregnation, the sample was dried at room temperature for 12 h, then at 80 °C for 12 h. Finally, the calcination was performed at 540 °C for 3 h. All the catalysts were prepared with the same amounts of WO_3 (20 wt%) and NiO (2.5 wt%). The prepared catalysts were designated as NiW-X (X=500, 560, 600 or 650), where X is the calcination temperature of MCM-41.

†To whom correspondence should be addressed.
E-mail: qiuzegang@sxicc.ac.cn, lfzhao@sxicc.ac.cn

2. Characterization Techniques

The thermogravimetric analysis and differential thermal analysis (TG-DTA) were recorded on a Rigaku Thermo plus Evo TG 8120 instrument at a heating rate of 10 °C·min^{-1} in air with a flow rate of 30 ml·min^{-1}.

The X-ray diffraction (XRD) was recorded on a Bruker D8 Advance diffractometer with Cu Kα radiation (λ=1.54178 Å). The power diffractograms were recorded in the 2θ range of 1.5-80° at a step of 0.01° s^{-1}.

N_2 adsorption-desorption isotherms were recorded on a Tristar-3000 Micromeritics volumetric apparatus. The special surface area was calculated according to the BET isothermal equation. The average pore diameter was calculated by applying the Barret-Joyner-Halenda method (BJH) to the adsorption branches of the N_2 isotherms. The pore volume was obtained for the isotherms at P/P_0=0.99.

The XPS spectra were measured by using a Kratos XSAM800 fitted with an Al Kα source (1486.6 eV) with two ultra-high-vacuum (UHV) chambers. The binding energy was referenced to the C1s peak (284.8 eV) to account for charging effects. The areas of the peaks were computed after fitting of the experimental spectra to Gaussian/Lorentzian curves and removal of the background (Shirley function). Surface atomic ratios were calculated from the peak area ratios normalized by the corresponding atomic sensitivity factors.

Laser Raman spectra were recorded on a LabRAM HR800 System with a CCD detector at room temperature. The 514 nm of the Ar^+ laser was employed as the exciting source with a power of 1 MW.

High resolution transmission electron microscopy (HRTEM) was performed using a JEOL (JEM-2100F). The calcined samples were suspended in ethanol with an ultrasonic dispersion for several minutes and deposited on the microscope grid.

IR spectra of adsorbed pyridine (Py-IR) were recorded using a Nicolet-510P apparatus. Prior to the pyridine adsorption, the calcined samples were pressed into thin wafers and evacuated in situ under vacuum at 300 °C for 2 h, then cooled to room temperature, and successive pyridine was dosed until saturated adsorption on the samples. Finally, the system was evacuated at different temperatures and pyridine adsorbed IR spectra were recorded.

3. Hydrodenitrogenation Measurement

The quinoline HDN reaction was carried out in a fixed-bed reactor (a 50 cm long stainless steel tube with an inner diameter of 6 mm) with the feed of quinoline in n-heptane (0.5 wt% N). The reactor was charged with 1 g catalyst in 20-40 mesh size. Prior to the reaction, the catalyst was in-situ presulfided at 400 °C and 3 MPa for 3 h with a 3 mL/h feed of 5% CS_2 in n-hexane. After that, the HDN reaction was carried out under the conditions (pressure of 4 MPa, temperature of 350-400 °C at a step of 10 °C, WHSV of 2 h^{-1} and H_2/feed volumetric ratio of 1000). After a stabilization period of 12 h, the reaction products were condensed and periodically separated from a gas-liquid separator. The reaction products were analyzed by a 5860 gas chromatograph equipped with a flame ionization detector and a capillary column (DB-5).

RESULTS AND DISCUSSION

1. Sample Characterizations

1-1. TG-DTA

The TG-DTA curve of the parent MCM-41, given in Fig. 1, is similar to those previously published [17,18]. The TG curve exhibits three distinct stages of weight loss 30-130 °C, 230-350 °C and above 350 °C. The first stage is due to the desorption of water. The second stage is associated with the combustion of the organic template species. The third stage is related to the water losses via condensation of the silanol groups. Also, there is nearly no weight loss at about 800 °C. From the inset curve (the magnifying figure of TG curve), the weight loss above 500, 560, 600 and 650 °C is 5.3%, 3.0%, 1.8% and 0.9%, respectively. It indicates that the weight loss is very small above 600 and 650 °C.

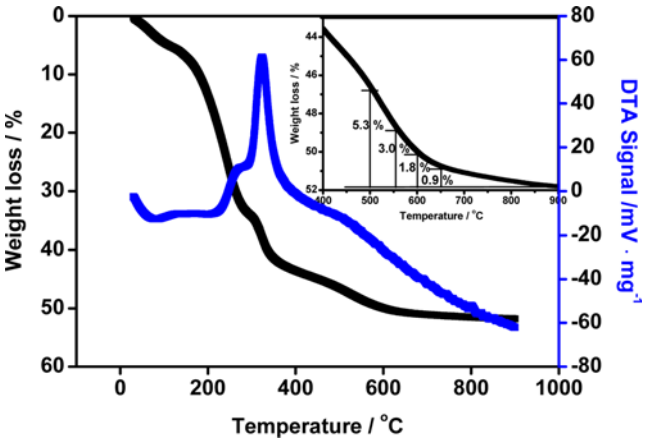

Fig. 1. TG-DTA curve of parent MCM-41.

1-2. XRD

Fig. 2 displays the small-angle XRD patterns of the MCM-41 which was calcined at different temperatures. The small-angle XRD patterns of all the MCM-41 have three peaks that can be indexed to (100), (110), (200) reflections, which correspond to a well ordered hexagonal pore system [19]. The result is confirmed by the nitrogen adsorption isotherms as shown in Fig. 4(a). Furthermore, the position of (100) peak slightly shifts to higher angle with the increase of MCM-41's calcination temperature, which may be related to the lattice contraction of MCM-41 during the higher temperature cal-

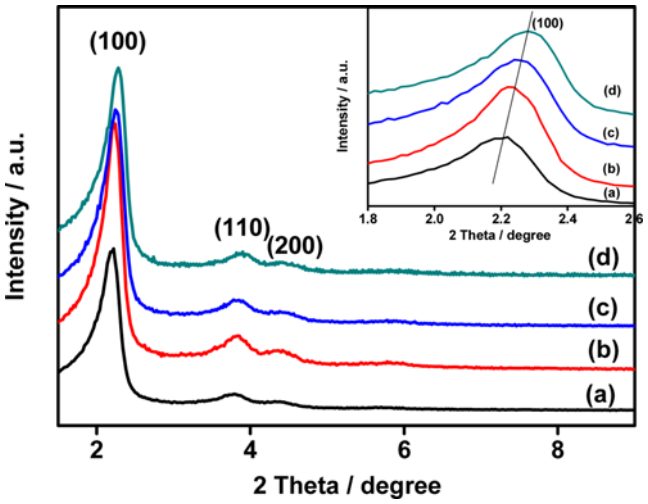

Fig. 2. Small-angle XRD patterns of the MCM-41: (a) MCM-500; (b) MCM-560; (c) MCM-600; (d) MCM-650.

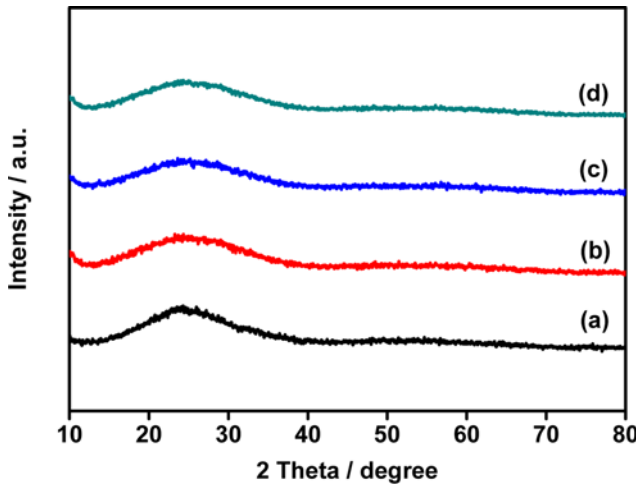

Fig. 3. Wide-angle XRD patterns of the catalysts: (a) NiW-500; (b) NiW-560; (c) NiW-600; (d) NiW-650.

cination [16].

The wide-angle XRD patterns of the catalysts, in Fig. 3, show that all the catalysts exhibit a very broad peak corresponding to the amorphous silica walls. No peaks related to Ni and W crystalline phases are detected in the XRD patterns of all the catalysts. These results reveal that the particle size of Ni and W crystallites is very small or they are highly dispersed on the support [20].

1-3. Nitrogen Adsorption-desorption

The textural properties of MCM-41 and the catalysts are listed in Table 1. MCM-500 shows the least specific surface area (S_{BET}), average pore diameter (Dp) and pore volume (Vp) among all the supports. It may be due to that a small quantity of organic fragments is still preserved within the pore structure [17]. Moreover, the S_{BET}, Dp and Vp of the MCM-41 increased with increase of the MCM-41's calcination temperature. However, Dp and Vp of the MCM-41 do not significantly vary (about 0.03 nm and 0.03 $cm^3 \cdot g^{-1}$) when it was calcined above 600 °C. This well agrees with Keene et al.

Table 1. Textural properties of the MCM-41 and catalysts

Sample	S_{BET}[a] ($m^2 \cdot g^{-1}$)	D_p[b] (nm)	V_p[c] ($cm^3 \cdot g^{-1}$)	NS_{BET}[d]
MCM-500	938.5	3.32	0.81	-
MCM-560	995.6	3.63	0.89	-
MCM-600	1038.3	3.69	0.92	-
MCM-650	1039.2	3.59	0.93	-
NiW-500	496.9	2.79	0.35	0.67
NiW-560	616.2	2.91	0.45	0.79
NiW-600	638.2	3.06	0.49	0.78
NiW-650	658.8	3.27	0.58	0.80

[a] S_{BET}, specific surface area calculated by the BET method

[b] D_p, average pore diameter corresponding to the maximum of the pore size distribution obtained from the adsorption isotherm by the BJH method

[c] V_p, pore volume determined by nitrogen adsorption at a relative pressure of 0.99

[d] $NS_{BET}=S_{BET\ of\ catalyst}/[(1-y)\times S_{BET\ of\ support}]$, y is the weight fraction of the metallic phases

[17] and the result of TG-DTA (a small weight loss above 600 °C). Furthermore, a significant decrease in the S_{BET} and Vp is observed when Ni and W species are impregnated to the MCM-41. In fact, the decrease in the S_{BET} is due to the dilution of the parent MCM-41 by Ni and W phases [21]. Also, the occupation and the blockage of pores by the metal particles may lead to the decrease in the S_{BET}. To confirm the blockage of MCM-41's pores, the normalized S_{BET} values are calculated using an equation proposed by Vradman et al. [21] (see Table 1).

$$NS_{BET}=S_{BET\ of\ catalyst}/[(1-y)\times S_{BET\ of\ support}]$$

where NS_{BET} is normalized S_{BET} and y is the weight fraction of the metallic phases. The value of NS_{BET} for the catalyst of NiW-500 is 0.67. However, the value of NS_{BET} for other catalysts is about 0.79 and higher than that of the NiW-500 (0.67). It indicates that the blockage of MCM-41's pores by Ni and W species for the catalyst of NiW-500 is the most significant one among all the catalysts. The result agrees with the nitrogen adsorption isotherms shown in Fig. 4(A).

The N_2 adsorption isotherms and pore size distribution of the MCM-41 and the catalysts are shown in Fig. 4(A) and (B). According to the literature [22], the sharpness of the step on the N_2 adsorption isotherms indicates the uniformity of mesopore size distribution. Fig. 4(A) and (B) show that all the MCM-41 present a type IV isotherm with an H1 hysteresis loop and a narrow pore size distribu-

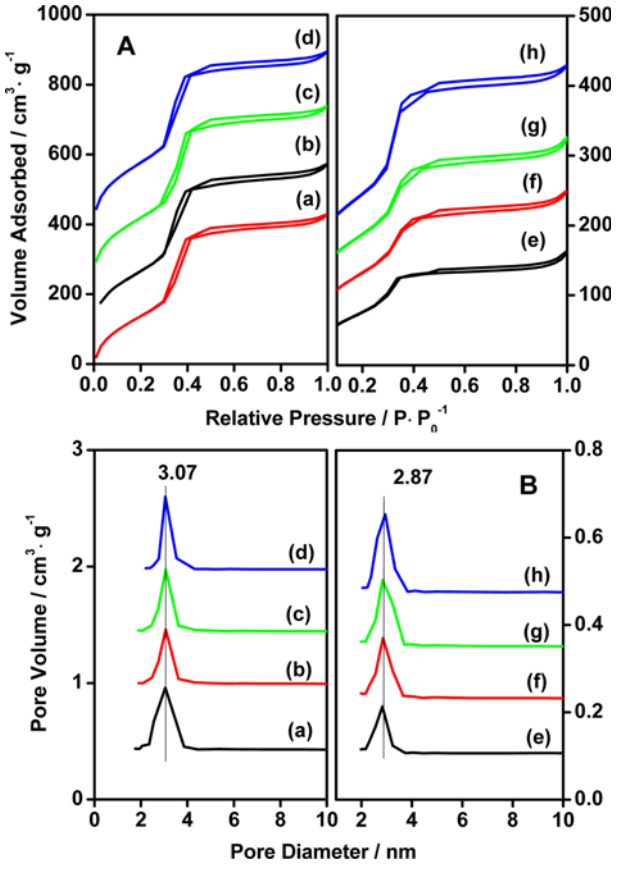

Fig. 4. N_2 adsorption-desorption isotherms (A) and Pore size distribution curves (B) of the MCM-41 and catalysts: (a) MCM-500; (b) MCM-560; (c) MCM-600; (d) MCM-650; (e) NiW-500; (f) NiW-560; (g) NiW-600; (h) NiW-650.

tion. However, the sharpness of the step (Fig. 4(A)) of the catalysts is much lower than that of the MCM-41, indicating the decrease of the uniformity of mesopore size distribution, especially for the catalyst of NiW-500. This may be due to the smallest pore diameter of MCM-500 (Table 1). Moreover, from Fig. 4(B), the pore size distribution slightly shifts to the lower pore diameter in the catalysts relative to MCM-41 supports, which reflects the formation of particles inside the pores [23].

1-4. XPS

XPS technique was performed to better understand the dispersion of W species. It is stated that the ratio of the metal-to-support from the XPS result can provide important information regarding the dispersion of the metal species [24]. Thus, the ratio of W/Si on the catalysts was calculated and the results are given in Table 2. The ratio of W/Si follows the order of NiW-650 (0.048)≈NiW-600 (0.046) >NiW-560 (0.042)>>NiW-500 (0.033). Therefore, the dispersion of W species follows the order of NiW-650≈NiW-600>NiW-560>> NiW-500. As stated in the section of N_2 adsorption-desorption, the S_{BET}, Dp and Vp of the MCM-41 increase with the increase of MCM-41's calcination temperature. The high S_{BET}, Dp and Vp of the MCM-41 may lead to the higher dispersion of W species. Furthermore, the high dispersion of W species may lead to the generation of more active species on the catalysts. Moreover, because the XPS technique is a kind of surface technique, the lowest ratio of W/Si for the catalyst of NiW-500 (0.033) may indicate that the W species are deposited inside the pores of the catalyst of NiW-500. This well agrees with the results of N_2 adsorption-desorption.

The chemical state and surface composition of catalysts are also revealed by XPS. The binding energies of the W4f and Ni2p are compiled in Table 2. The W4f core level spectra of all the catalysts show a $W4f_{7/2}$ and $W4f_{5/2}$ doublet centered at binding energy (BE) about 35.8 eV and 38.0 eV, respectively. Similarly, the Ni2p core level spectra of all the catalysts show a $Ni2p_{3/2}$ and $Ni2p_{1/2}$ doublet centered at BE about 856.0 eV and 873.8 eV, with the corresponding shake-up satellite at BE about 862.3 eV and 880.6 eV. Therefore, W4f and Ni2p XPS spectra of all the catalysts have similar peak shape at similar binding energy. According to the literature, the BE of $W4f_{7/2}$ spectrum in the range of 35.8-36.5 eV is ascribed to WO_3 and/or $NiWO_4$ [6], and the BE of $Ni2p_{3/2}$ spectrum in the range of 855.7-856.5 eV is ascribed to Ni_2O_3 and /or $NiWO_4$ [25].

1-5. Raman

The Raman spectra are given in Fig. 5. According to the literature, MCM-41 does not present Raman band [26]. The crystalline WO_3 presents the bands of 803, 710 and 274 cm^{-1} [27]. In addition, the band at 970 cm^{-1} is assigned to the symmetric stretching of the W=O band in octahedrally coordinated W species [20].

Table 2. The binding energies of the W4f, Ni2p and the ratios of W/Si

Catalyst	Binding energy/eV				W/Si
	$W4f_{7/2}$	$W4f_{5/2}$	$Ni2p_{3/2}$	$Ni2p_{1/2}$	
NiW-500	35.9	38.0	856.0	873.7	0.033
			862.2	880.8	
NiW-560	35.8	37.9	856.0	873.8	0.042
			862.3	880.3	
NiW-600	35.8	38.0	856.2	874.1	0.046
			862.5	880.6	
NiW-650	35.9	37.9	856.1	874.0	0.048
			862.4	881.3	

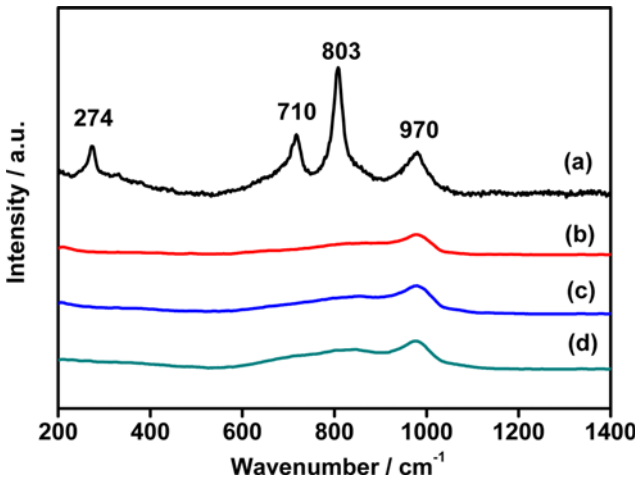

Fig. 5. Raman spectra of the catalysts: (a) NiW-500; (b) NiW-560; (c) NiW-600; (d) NiW-650.

Fig. 5 shows that several strong Raman bands assigned to crystalline WO_3 (803, 710 and 274 cm^{-1}) are observed for the catalyst of NiW-500, indicating the poor dispersion of the W species on the catalyst of NiW-500. However, no Raman bands assigned to crystalline WO_3 (803, 710 and 274 cm^{-1}) are observed for other catalysts, indicating good dispersion of the W species on the catalysts of NiW-560, NiW-600 and NiW-650. Therefore, it is inferred that the catalyst of NiW-500 shows the worst dispersion of W species. This is agrees well with the result of XPS discussed above. However, based on the aforementioned results of wide-angle XRD, no crystalline phases due to WO_3 are detected in the wide-angle XRD patterns of NiW-500 catalyst. This discrepancy may be attributed to the fact that the WO_3 crystal size is below the detection limit of the XRD technique.

Fig. 5 also shows that a band at 970 cm^{-1} is observed for all the catalysts, suggesting the presence of octahedrally coordinated W species on all the catalysts. Therefore, both crystalline WO_3 and octahedrally coordinated W species coexist on the catalyst of NiW-500. However, only octahedrally coordinated W species are present on other catalysts. The octahedrally coordinated W species are the genesis of active species for hydrotreating catalyst [28]. Hence, it can be concluded that the support of the MCM-41 which was calcined at higher temperature favors the formation of the appropriate nature of W species on the catalysts.

1-6. HRTEM

To further investigate the dispersion of metallic species, the HRTEM characterization was carried out. The HRTEM spectra of all catalysts are shown in Fig. 6. It is confirmed that the average size of the metallic oxide particles is below 4 nm for all the catalysts, which is in accordance with the results of XRD. From Fig. 6 it is also observed that the metallic oxide particles exist in the form of aggregates on the catalyst of NiW-500, whereas the metallic oxide particles are well dispersed on other catalysts. As stated above about N_2 adsorption-desorption, the MCM-500 shows the least S_{BET}, Dp and

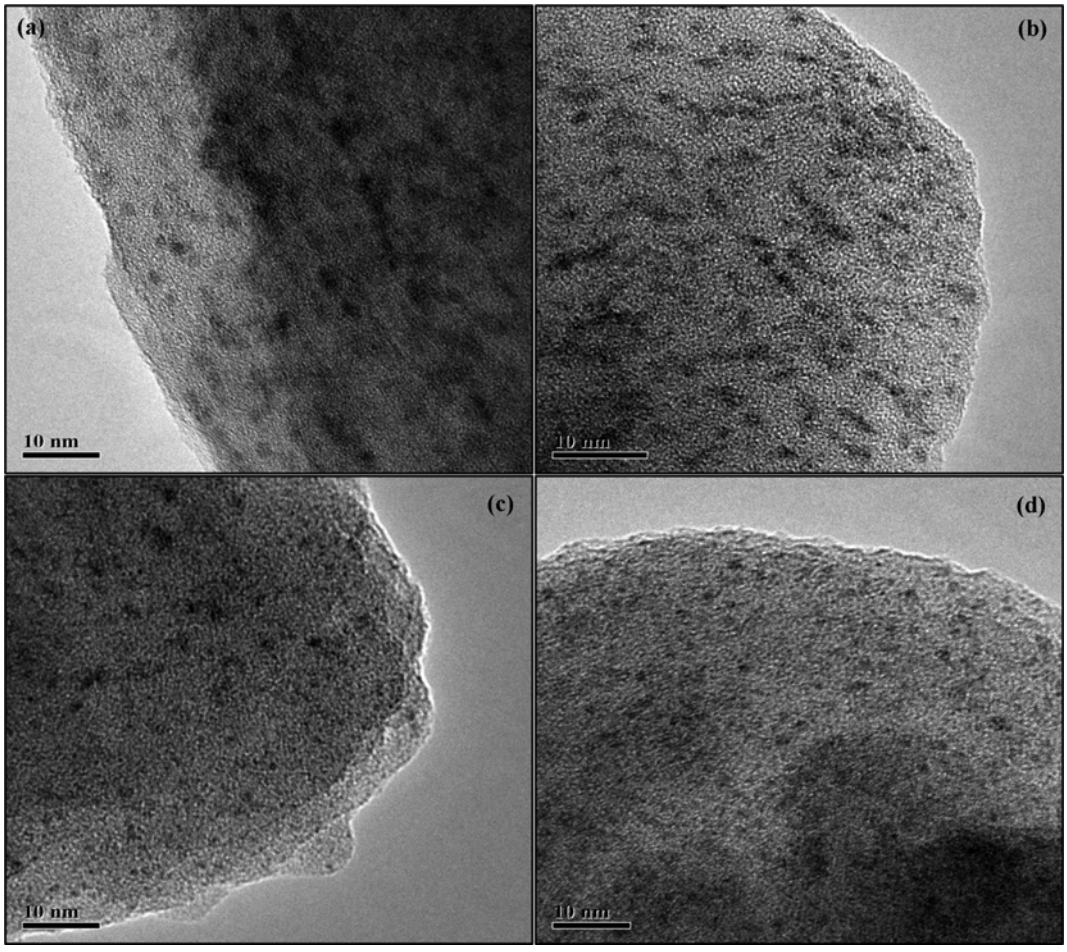

Fig. 6. HRTEM micrographs for (a) NiW-500; (b) NiW-560; (c) NiW-600; (d) NiW-650.

Vp among all the supports. These results demonstrate that the dispersion of metallic oxide particles is influenced by the textural properties of support.

1-7. Py-IR

The surface acidity of catalysts was determined by the in situ Py-IR technique. Usually, the bands at approximately 1,446, 1.575, 1,595 and 1,608 cm^{-1} are assigned to Lewis acid sites, while the bands at around 1,540 and 1,636 cm^{-1} are assigned to Brönsted acid sites. In addition, the band at 1,490 cm^{-1} can be associated with pyridine adsorbed on both Lewis and Brönsted acid sites [29]. The Py-IR spectra of catalysts are presented in Fig. 7, which clearly reveals that both Lewis and Brönsted acid sites coexist on the surface of all the catalysts. The density of acid sites on the surface of the catalysts at different temperatures is listed in Table 3.

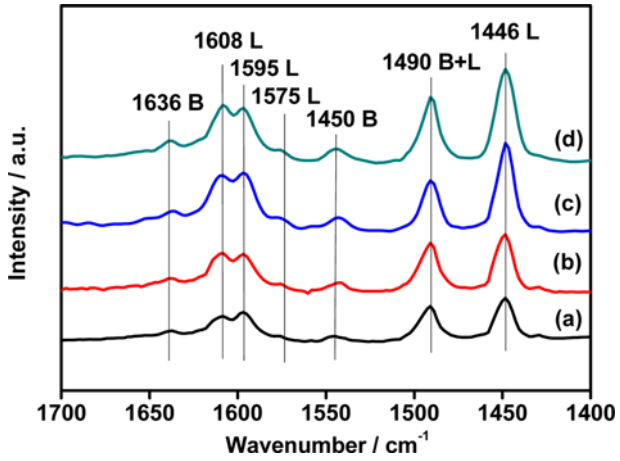

Fig. 7. Py-IR spectra of the catalysts: (a) NiW-500; (b) NiW-560; (c) NiW-600; (d) NiW-650.

Clearly, the density of both Lewis and Brönsted acid sites on the surface of catalysts follows the order of NiW-650≈NiW-600>NiW-

Table 3. Acidity results for the NiW catalysts measured by FT-IR spectroscopy combined with pyridine desorption at different temperatures

Catalyst	Brönsted acidity/ μmol pyridine g^{-1}				Lewis acidity/ μmol pyridine g^{-1}			
	Temperature/°C				Temperature/°C			
	40	100	200	250	40	100	200	250
NiW-500	15.8	16.2	5.5	5.0	249.7	117.3	39.6	22.0
NiW-560	24.6	27.3	10.0	6.1	285.0	171.1	59.9	37.5
NiW-600	24.9	33.9	18.1	6.8	333.6	205.4	81.5	53.3
NiW-650	32.2	36.3	19.3	7.0	345.7	210.6	87.6	59.7

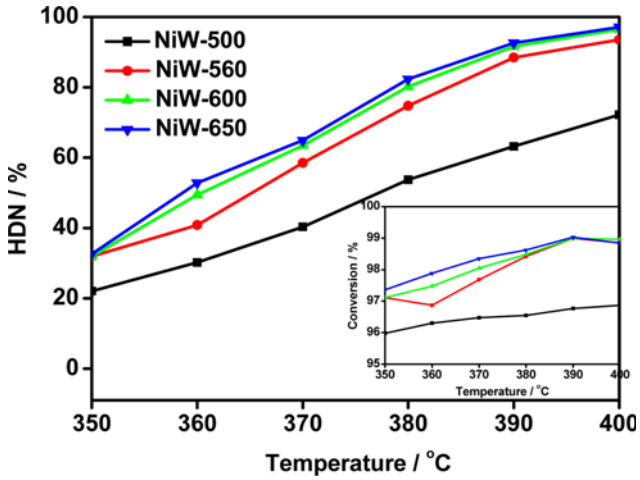

Fig. 8. Conversion and HDN activity of quinoline as a function of reaction temperature for NiW catalysts. Reaction conditions: P=4 MPa, H_2/feed=1,000, WHSV=2 h^{-1}.

560>NiW-500. As mentioned above, the S_{BET}, Dp and Vp of the MCM-41 increase with increase of the MCM-41's calcination temperature. The high S_{BET}, Dp and Vp of the MCM-41 may lead to the generation of more acid sites on the catalysts.

2. Hydrodenitrogenation

Catalytic activity was evaluated in the reaction for HDN of quinoline and the results for all the catalysts are compared in Fig. 8 as a function of the reaction temperature. It clearly shows that the conversion of quinoline is about 95-99% in the range of reaction temperature investigated for all the catalysts. It indicates that quinoline could be hydrogenated easily to hydrogenation products. Fig. 8 also shows that the HDN activity for all the catalysts increases with the increase in the reaction temperature. It indicates that this reaction is activation energy demanding [30]. In addition, the HDN activity of the catalysts follows the order of NiW-650≈NiW-600>NiW-560>NiW-500. It is well accepted that the high dispersion of metallic species on the surface of the support is essential for the good performance of hydrotreating catalysts, and that the surface properties of support affect the dispersion and the local environment of the metal species [14,31]. As stated previously, the S_{BET}, Dp and Vp of the MCM-41 increase with the increase in the MCM-41's calcination temperature. The high S_{BET}, Dp and Vp of the MCM-41 favor the dispersion of active species, the formation of the appropriate nature of W species and acid sites on the catalysts. Therefore, it is not surprising that the HDN activity follows the order of NiW-650≈NiW-600>NiW-560>NiW-500. Because the HDN activity of the catalysts of NiW-600 is similar to that of the catalysts of NiW-650, the temperature of 600 ℃ is selected as the optimum calcination temperature for the HDN of quinoline in order to save energy during the calcination process.

The HDN reaction network of quinoline is presented in Fig. 9. In general, there are two ways to remove the nitrogen atom from quinoline, via OPA (aromatic intermediates pathway) or DHQ (saturated intermediates pathway) (Fig. 9) [32]. It has been demonstrated that the PCH/PB ratio can roughly represent the relative selectivity of the two pathways [33].

Q, quinoline; THQ5, 5,6,7,8-tetrahydroquinoline; DHQ, decahydroquinoline; THQ1, 1,2,3,4-tetrahydroquinoline; OPA, ortho-propylaniline; PCHA, 2-propylcyclo-hexylamine; PCHE, propylcyclohexene; PCH, propylcyclohexane; PB, propylbenzene.

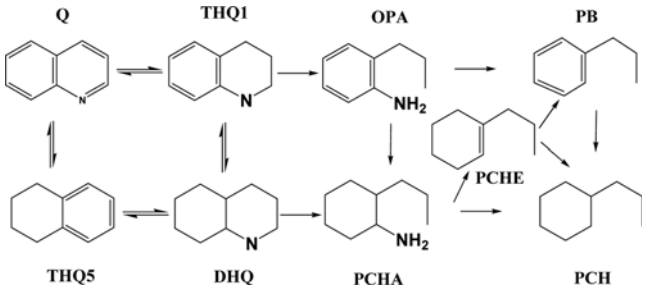

Fig. 9. HDN reaction network of quinoline.

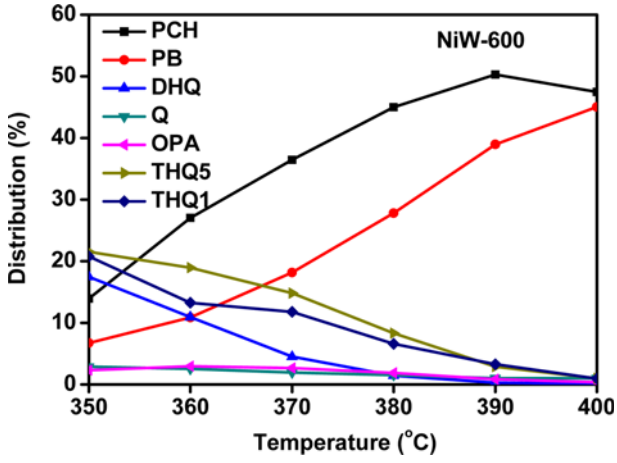

Fig. 10. Product distribution for HDN of quinoline as a function of reaction temperature for catalyst of NiW-600. Reaction conditions: P=4 MPa, H_2/feed=1,000, WHSV=2 h^{-1}.

We chose the catalyst of NiW-600 as an example to show the product distribution for HDN of quinoline because the product distribution is similar for all the catalysts (see Fig. 10). The main products

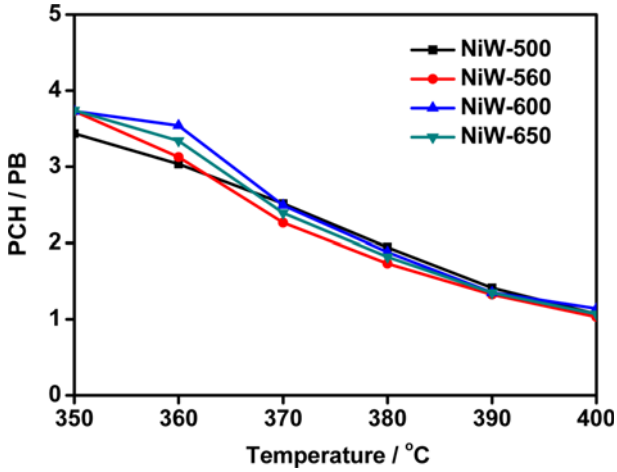

Fig. 11. The ratio of PCH/PB as a function of reaction temperature for NiW catalysts. Reaction is conducted at P=4 MPa, H_2/feed=1,000, WHSV=2 h^{-1}.

are THQ1, THQ5, DHQ, PCH and PB. The selectivity of OPA and PCHA is negligible, revealing that the further reaction rate of OPA and PCHA is faster than their formation rate. With increasing of the reaction temperature, the C-N band cleavage is accelerated, leading to the continuously decreased selectivity of THQ1, THQ5 and DHQ, and the continuously increased selectivity of the final products of PB and PCH. However, it can be seen from Fig. 11 that the PCH/PB ratio continuously decreases with increasing of the reaction temperature. This is well agrees with Cocchetto [34]. The reason may be that the C-N band cleavage is significantly accelerated with increasing reaction temperature, but the hydrogenation reaction is inhibited at the high reaction temperature because it is an exothermic reaction.

The ratios of PCH/PB for HDN of quinoline over different catalysts are presented in Fig. 11. It is noted that the ratio of PCH/PB is very similar for all the catalysts, suggesting that the relative selectivity of the HDN pathways for quinoline is not influenced by the calcination temperature of MCM-41.

CONCLUSION

MCM-41 was calcined at 500, 560 600 or 650 °C and used as support for NiW catalysts. The surface area, the pore volume and the average pore diameter of the MCM-41 increased with the increasing of the MCM-41's calcination temperature. Thus, the dispersion of W species, the active species and the acid sites on the catalysts were improved. The catalytic performance of the NiW catalysts was tested by the HDN of quinoline in the temperature range of 350-400 °C. The results showed that the relative selectivity of HDN pathways was similar for all the catalysts. However, the HDN activity followed the order of NiW-650≈NiW-600>NiW-560 >NiW-500. The increase of HDN activity was ascribed to the higher dispersion of the W species, the appropriate nature of W species and the more acid sites on the catalysts. Since the similar HDN activity of the catalysts of NiW-600 and NiW-650, the temperature of 600 °C was selected as the optimum calcination temperature in order to save energy during calcination process.

ACKNOWLEDGEMENTS

Supported by the "Strategic Priority Research Program" Demonstration of Key Technologies for Clean and Efficient Utilization of Low-rank Coal (Grant No. XDA07020200) as well as the Local Cooperation Programs of the Chinese Academy of Sciences (XBXJ-2011-007).

REFERENCES

1. M. A. Domínguez-Crespo, A. M. Torres-Huerta, L. Díaz-García, E. M. Arce-Estrada and E. Ramírez-Meneses, *Fuel Process. Technol.*, **89**, 788 (2008).
2. K. K. Soni, K. C. Mouli, A. K. Dalai and J. Adiaye, *Micropor. Mesopor. Mater.*, **152**, 224 (2012).
3. E. Peeters, M. Cattenot, C. Geantet, M. Breysse and J. L. Zotin, *Catal. Today*, **133-135**, 299 (2008).
4. Y. Z. Luan, Q. M. Zhang, D. M. He, J. Guan and C. H. Liang, *Asia-Pac. J. Chen. Eng.*, **4**, 704 (2009).
5. H. A. Al-Megren, S. L. González-Cortés, T. Xiao and M. L. H. Green, *Appl. Catal. A: Gen.*, **329**, 36 (2007).
6. G. Q. Cui, J. F. Wang, H. F. Fan, X. Y. Sun, Y. Jiang, S. J. Wang, D. Liu and J. Z. Gui, *Fuel Process. Technol.*, **92**, 2320 (2011).
7. S. Z. Li and J. S. Lee, *J. Catal.*, **173**, 134 (1998).
8. P. Clark, W. Li and S. T. Oyama, *J. Catal.*, **200**, 140 (2001).
9. Y. Fan, X. J. Bao, H. Wang, C. F. Chen and G. Shi, *J. Catal.*, **245**, 477 (2007).
10. M. B. Güemez, J. F. Canbra, P. L. Arias, J. A. Legarreta and J. L. G. Fierro, *Fuel*, **74**, 285 (1995).
11. X. P. Duan, X. Li, A. J. Wang, Y. Teng, Y. Wang and Y. K. Hu, *Catal. Today*, **149**, 11 (2010).
12. M. H. Lu, A. J. Wang, X. Li, X. P. Duan, Y. Teng, Y. Wang, C. S. Song and Y. K. Hu, *Energy Fuels*, **21**, 554 (2007).
13. S. J. Sardhar Basha, P. Vijayan, C. Suresh, D. Santhanaraj and K. Shanthi, *Ind. Eng. Chem. Res.*, **48**, 2774 (2009).
14. S. J. Sardhar Basha, P. Vijayan, C. Suresh, D. Santhanaraj and K. Shanthi, *Appl. Catal. A: Gen.*, **308**, 91 (2006).
15. A. E. R. S. Khder, H. M. A. Hassan and M. S. El-Shall, *Appl. Catal. A: Gen.*, **411-412**, 77 (2012).
16. C. Y. Chen, H. X. Li and M. E. Davis, *Microporous Mater.*, **2**, 17 (1993).
17. M. T. J. Keene, R. D. M. Gougeon, R. Denoyel, R. K. Harris, J. Rouquerol and P. L. Llewellyn, *J. Mater. Chem.*, **9**, 2843 (1999).
18. S. Vetrivel and A. Pandurangan, *J. Mater. Chem. A: Chemical*, **227**, 269 (2005).
19. E. Kraleva, M. L. Saladina, A. Spinella, G. Nasillo and E. Caponetti, *J. Mater. Sci.*, **46**, 7114 (2011).
20. K. Soni, P. E. Boahene, K. C. Mouli, A. K. Dalai and J. Adjaye, *Appl. Catal. A: Gen.*, **398**, 27 (2011).
21. L. Vradman, M. V. Landau, D. Kantorovich, Y. Koltypin and A. Gedaken, *Microporous Mesoporous Mater.*, **79**, 307 (2005).
22. Y. M. Luo, Z. Y. Hou, R. T. Li and X. M. Zheng, *Microporous Mesoporous Mater.*, **109**, 585 (2008).
23. L. Vradman, M. V. Landau, M. Herskowitz, V. Ezersky, M. Talianker, S. Nikitenko, Y. Koltypin and A. Gedanken, *J. Catal.*, **213**, 163 (2003).
24. J. J. Lee, H. Kim, J. H. Koh, A. Jo and S. H. Moon, *Appl. Catal. B: Environ.*, **58**, 89 (2005).
25. S. J. Lawrence, L. E. Makovsky, J. E. Stencel, F. R. Brown and D. M. Hercules, *J. Phys. Chem.*, **85**, 3700 (1981).
26. H. Chen, W. L. Dai, J. F. Deng and K. N. Fan, *Catal. Lett.*, **81**, 131 (2002).
27. D. S. Kim, M. Ostromecki and I. E. Wachs, *Catal. Lett.*, **33**, 209 (1995).
28. Z. P. Lei, L. J. Gao, H. F. Shui, W. L. Chen, Z. C. Wang and S. B. Ren, *Fuel Process. Technol.*, **92**, 2055 (2011).
29. P. Kalita, N. M. Gupta and R. Kumar, *J. Catal.*, **245**, 338 (2007).
30. C. Sursh, D. Santhanaraj, M. Gurulakshmi, G. Deepa, M. Selvaraj, N. R. S. Rekha and K. Shanthi, *ACS Catal.*, **2**, 127 (2012).
31. X. Li, A. J. Wang, Z. C. Sun, C. Li, J. Ren, B. Zhao, Y. Wang, Y. Y. Chen and Y. K. Hu, *Appl. Catal. A: Gen.*, **254**, 319 (2003).
32. M. Jian and R. Prins, *J. Catal.*, **179**, 18 (1998).
33. R. Prins, M. Jian and M. Flechsenhar, *Polyhedron*, **16**, 3235 (1997).
34. J. F. Cocchetto and C. N. Satterfield, *Ind. Eng. Chem. Process. Des.*, **20**, 49 (1981).